High-performance coherent population trapping clock with polarization modulation

Peter Yun[1],* François Tricot[1], Claudio Eligio Calosso[2], Salvatore Micalizio[2],
Bruno François[3], Rodolphe Boudot[3], Stéphane Guérandel[1], and Emeric de Clercq[1]
[1] *LNE-SYRTE, Observatoire de Paris, PSL Research University, CNRS, Sorbonne Universités, UPMC Univ. Paris 06, 61 avenue de l'Observatoire, 75014 Paris, France*
[2] *Istituto Nazionale di Ricerca Metrologica, INRIM, Strada delle Cacce 91, 10135 Torino, Italy and*
[3] *FEMTO-ST, CNRS, UFC, 26 chemin de l'Épitaphe 25030 Besançon Cedex, France*
(Dated: December 29, 2016)

We demonstrate a vapor cell atomic clock prototype based on continuous-wave (CW) interrogation and double-modulation coherent population trapping (DM-CPT) technique. The DM-CPT technique uses a synchronous modulation of polarization and relative phase of a bi-chromatic laser beam in order to increase the number of atoms trapped in a dark state, *i.e.* a non-absorbing state. The narrow resonance, observed in transmission of a Cs vapor cell, is used as a narrow frequency discriminator in an atomic clock. A detailed characterization of the CPT resonance versus numerous parameters is reported. A short-term fractional frequency stability of $3.2 \times 10^{-13}\tau^{-1/2}$ up to 100 s averaging time is measured. These performances are more than one order of magnitude better than industrial Rb clocks and comparable to those of best laboratory-prototype vapor cell clocks. The noise budget analysis shows that the short and mid-term frequency stability is mainly limited by the power fluctuations of the microwave used to generate the bi-chromatic laser. These preliminary results demonstrate that the DM-CPT technique is well-suited for the development of a high-performance atomic clock, with potential compact and robust setup due to its linear architecture. This clock could find future applications in industry, telecommunications, instrumentation or global navigation satellite systems.

I. INTRODUCTION

Microwave Rb vapor-cell atomic clocks [1], based on optical-microwave double resonance, are today ubiquitous timing devices used in numerous fields of industry including instrumentation, telecommunications or satellite-based navigation systems. Their success is explained by their ability to demonstrate excellent short-term fractional frequency stability at the level of $10^{-11}\tau^{-1/2}$, combined with a small size, weight, power consumption and a relatively modest cost. Over the last decade, the use of narrow-linewidth semiconductor lasers and the demonstration of advanced atom interrogation techniques, has led to the development in laboratories of new-generation vapor cell clocks [2–5]. For instance the pulsed-optical-pumping (POP) clock uses a pulsed microwave interrogation, together with a pulsed pumping and detection. Such clocks have achieved a 100-fold improvement in frequency stability compared to existing commercial vapor cell clocks.

Among the clocks based on advanced interrogation techniques, clocks based on a quantum interference phenomenon named coherent population trapping (CPT) have proven to be promising alternative candidates. Since its discovery in 1976 [6], coherent population trapping physics [7–10] has motivated stimulating studies in various fields covering fundamental and applied physics such as slow-light experiments [11], high-resolution laser spectroscopy, magnetometers [12, 13], laser cooling [14] or atomic frequency standards. Basically, CPT occurs by connecting two long-lived ground state hyperfine levels of an atomic specie to a common excited state by simultaneous action of two resonant optical fields. When both optical fields are resonant or close to the resonance, and at null Raman detuning, i.e., when the frequency difference between both optical fields matches perfectly the atomic ground-state hyperfine frequency, atoms are trapped through a destructive quantum interference process into a noninteracting coherent superposition of both ground states, so-called dark state, resulting in a clear decrease of the light absorption or equivalently in a net increase of the transmitted light. The output resonance signal, whose line-width is ultimately limited by the CPT coherence lifetime, can then be used as a narrow frequency discriminator towards the development of an atomic frequency standard. In a CPT-based clock, unlike the traditional double-resonance Rb clock [15], the microwave signal used to probe the hyperfine frequency is directly optically carried allowing to remove the microwave cavity and potentially to shrink significantly the clock dimensions.

The application of CPT to atomic clocks was firstly demonstrated in a sodium atomic beam [16, 17]. In 1993, N. Cyr et al proposed a simple method to produce a microwave clock transition in a vapor cell with purely optical means by using a modulated diode laser [18], demonstrating its high-potential for compactness. In 2001, a first remarkably compact atomic clock prototype was demonstrated in NIST [19, 20]. Further integration was achieved later thanks to the proposal [21] and development of micro-fabricated alkali vapor cells

* E-mail: enxue.yun@obspm.fr, permanent e-mail: yunenxue@163.com

[22], leading to the demonstration of the first chip-scale atomic clock prototype (CSAC) [23] and later to the first commercially-available CSAC [24]. Nevertheless, this extreme miniaturization effort induces a typical fractional frequency stability limited at the level of $10^{-10}\tau^{-1/2}$, not compliant with dedicated domains requiring better stability performances. In that sense, in the frame of the European collaborative MClocks project [25], significant efforts have been pursued to demonstrate compact (i.e., cm-scale cell instead of mm-scale as in CSAC) high-performance CPT-based atomic clocks and to help to push this technology to industry.

In standard CPT clocks, a major limitation to reach better frequency stability performances is the low contrast (C, the amplitude-to-background ratio) of the detected CPT resonance. This low contrast is explained by the fact that atoms interact with a circularly polarized bichromatic laser beam, leading most of the atomic population into extreme Zeeman sub-levels of the ground state, so called "end-states". Several optimized CPT pumping schemes, aiming to maximize the number of atoms participating to the clock transition (the 0-0 magnetically insensitive transition), have been proposed in the literature to circumvent this issue ([26, 27], and references therein), but at the expense of increased complexity.

In that sense, a novel constructive polarization modulation CPT [28] pumping technique, named double-modulation (DM) scheme, was recently proposed. It consists to apply a phase modulation between both optical components of the bichromatic laser synchronously with a polarization modulation. The phase modulation is needed to ensure a common dark state to both polarizations, allowing to pump a maximum number of atoms into the desired magnetic-field insensitive clock state. Compared to the push-pull optical pumping [29–31] or the lin⊥lin technique [32, 33], this elegant solution presents the main advantage of avoiding any optical beam separation or superposition and is consequently well-adapted to provide a compact and robust linear architecture setup.

In this article, we demonstrate a high-performance CW-regime CPT clock based on the DM technique. Optimization of the short-term frequency stability is performed by careful characterization of the CPT resonance versus relevant experimental parameters. A short-term frequency stability at the level of $3.2 \times 10^{-13}\tau^{-1/2}$ up to 100 s, comparable to best vapor cell frequency standards, is reported. A detailed noise budget is given, highlighting a dominant contribution of the microwave power fluctuations. Section II describes the experimental setup. Section III reports the detailed CPT resonance spectroscopy versus experimental parameters. Section IV reports best short-term frequency stability results. Noise sources limiting the stability are carefully analysed. In section V, we study the clock frequency shift versus each parameter and estimate the limitation of the clock mid-term frequency stability. In the supplemental material [34], part of the signal optimization and noise analysis for mid-term stability are presented in detail.

II. EXPERIMENTAL SET-UP

A. Optical set-up

Our setup is depicted in Fig. 1. A DFB laser diode emits a monochromatic laser beam around 895 nm, the wavelength of the Cs D_1 line. With the help of a fiber electro-optic phase modulator (EOPM), modulated at 4.6 GHz with about 26 dBm microwave power, about 70% of the carrier power is transferred into both first-order sidebands used for CPT interaction. The phase between both optical sidebands, so-called Raman phase in the following, is further modulated through the driving 4.6 GHz microwave signal. Two acousto-optic modulators (AOMs) are employed. The first one, AOM1, is used for laser power stabilization. The second one, AOM2, allows to compensate for the buffer-gas induced optical frequency shift ($\approx$ 160 MHz) in the CPT clock cell. A double-modulated laser beam is obtained by combining the phase modulation with a synchronized polarization modulation performed thanks to a liquid crystal polarization rotator (LCPR). The laser beam is expanded to 9 mm × 16 mm before the vapor cell. The cylindrical Cs vapor cell, 25 mm diameter and 50 mm long, is filled with 15 Torr of mixed buffer gases (argon and nitrogen). Unless otherwise specified, the cell temperature is stabilized to about 35 °C. A uniform magnetic field of 3.43 µT is applied along the direction of the cell axis by means of a solenoid to remove the Zeeman degeneracy. The ensemble is surrounded by two magnetic shields in order to reject the Earth and other stray magnetic fields.

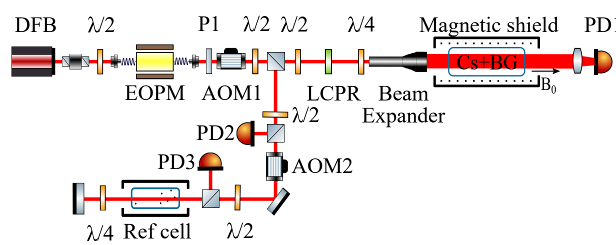

FIG. 1. Optical setup for DM CPT, where the abbreviations stand for: DFB distributed feedback diode laser, EOPM electro-optic phase modulator, LCPR liquid crystal polarization rotator, AOM acousto-optic modulator, P polarizer, $\lambda/2(4)$ half(quarter)-wave plate, BG buffer gas, PD photodiode.

B. Fiber EOPM sidebands generation

We first use a Fabry-Perot cavity to investigate the EOPM sidebands power ratio versus the coupling 4.596 GHz microwave power ($P_{\mu w}$), see Fig. 2. We choose

$P_{\mu w}$ around 26 dBm to maximize the power transfer efficiency into the first-order sidebands. The sidebands spectrum is depicted in the inset of Fig. 2.

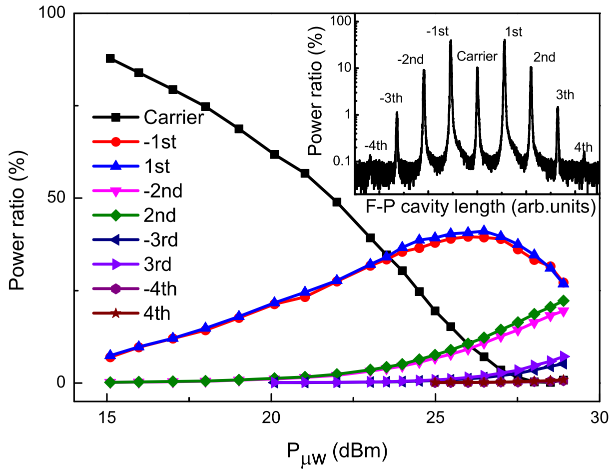

FIG. 2. Fractional power of laser sidebands at the EOPM output as a function of 4.596 GHz microwave power. Inset, the laser sidebands spectrum with $P_{\mu w} = 26.12$ dBm obtained by scanning the FP cavity length, notice the log scale of the y-axis.

C. Laser power locking

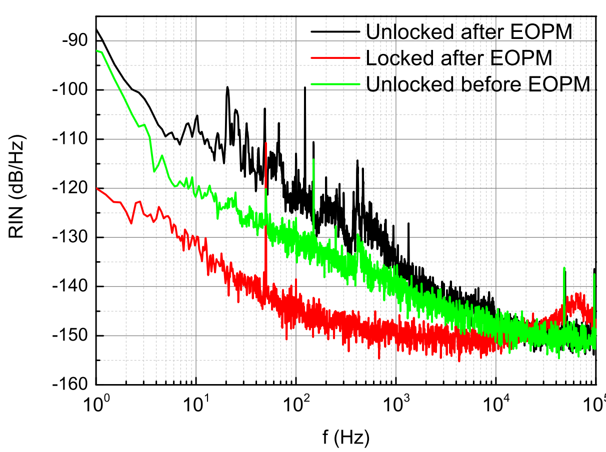

FIG. 3. Power spectral density of the laser RIN with (red) and w/o (black) power locking after the EOPM, the RIN measured before the EOPM is plotted in green.

Since the laser intensity noise is known as being one of the main noise sources which limit the performances of a CPT clock [10, 31], the laser power needs to be carefully stabilized. For this purpose, a polarization beam splitter (PBS) reflects towards a photo-detector a part of the laser beam, the first-order diffracted by AOM1 following the EOPM. The output voltage signal is compared to an ultra-stable voltage reference (LT1021). The correction signal is applied on a voltage variable power attenuator set on the feeding RF power line of the AOM1 with a servo bandwidth of about 70 kHz. The out-loop laser intensity noise (RIN) is measured just after the first PBS with a photo-detector (PD). The spectrum of the resulting RIN with and w/o locking is shown in Fig. 3. A 20 dB improvement at $F_M = 125$ Hz (LO modulation frequency for clock operation) is obtained in the stabilized regime.

It is worth noting that the DFB laser diode we used, with a linewidth of about 2 MHz, is sensitive even to the lowest levels of back-reflections [35], e.g., the coated collimated lens may introduce some intensity and frequency noise at the regime of 0.1 kHz to 10 kHz. Finding the correct lens alignment to minimize the reflection induced noise while keeping a well-collimated laser beam was not an easy task. To reduce light feedback from the EOPM fiber face, we use a 60 dB isolator before the EOPM. Even so, we still found that the EOPM induces additional intensity noise, as reported in Fig. 3 showing the RIN measured before (in green) and after (in black) the EOPM. Nevertheless, thanks to the laser power locking, we can reduce most of these noises by at least 15 dB in the range of 1 Hz to 1 kHz.

D. Laser frequency stabilization

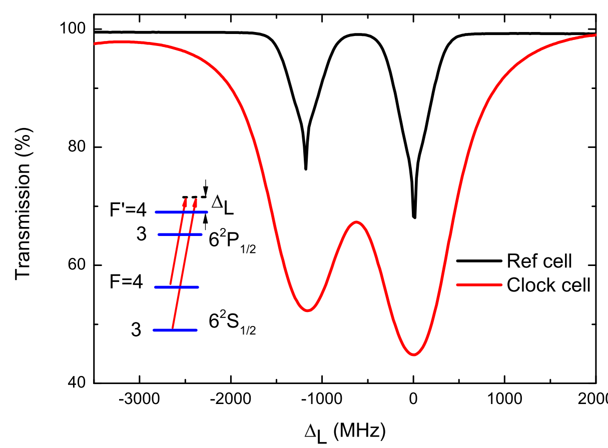

FIG. 4. Spectrum of the Cs D_1 line in the vacuum reference cell and in the clock cell recorded with the bichromatic laser. The optical transitions in the clock cell are broadened and shifted by collisions between the Cs atoms and buffer-gas molecules. The frequency shift is compensated by the AOM. The two absorptions from left to right correspond to the excited level $|6^2P_{1/2}, F' = 3\rangle$ and $|6^2P_{1/2}, F' = 4\rangle$, respectively. For the reference cell signal: laser power 0.74 mW, beam diameter 2 mm, cell temperature 22 °C, AOM frequency 160 MHz. The inset shows the atomic levels involved in D_1 line of Cesium.

Our laser frequency stabilization setup, similar to [31, 36], is depicted in Fig. 1. We observe in a vacuum cesium cell the two-color Doppler-free spectrum depicted in Fig. 4. The bi-chromatic beam, linearly polarized, is

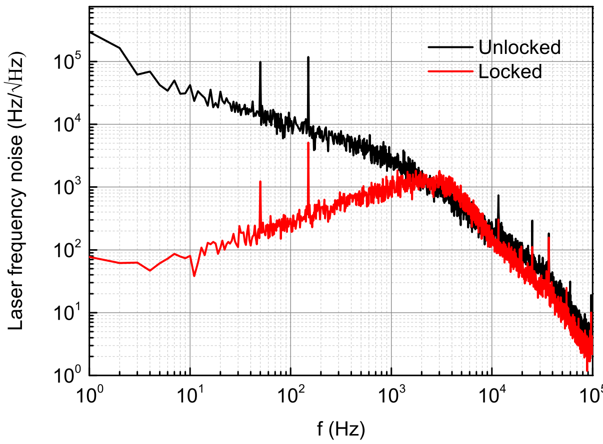

FIG. 5. The laser frequency noise measured on the error signal of the Doppler-free spectrum with and w/o frequency locking.

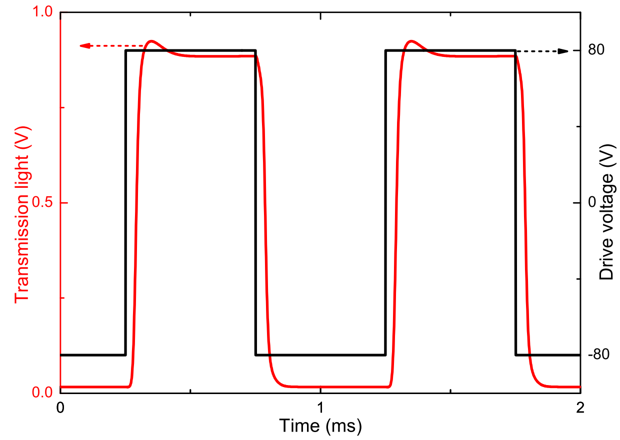

FIG. 6. LCPR response.

retro-reflected after crossing the cell with the orthogonal polarization. Only atoms of null axial velocity are resonant with both beams. Consequently, CPT states built by a beam are destroyed by the reversed beam, leading to a Doppler-free enhancement of the absorption [36].

The laser frequency detuning $\Delta_L = 0$ in Fig. 4 corresponds to the laser carrier frequency tuned to the center of both transitions $|6^2S_{1/2}, F = 3\rangle \rightarrow |6^2P_{1/2}, F' = 4\rangle$ and $|6^2S_{1/2}, F = 4\rangle \rightarrow |6^2P_{1/2}, F' = 4\rangle$ in D_1 line of Cesium, where F is the hyperfine quantum number. For this record, the microwave frequency is 4.596 GHz, half the Cs ground state splitting, and the DFB laser frequency is scanned. We measured the frequency noise by utilizing the error signal of the Doppler-free spectrum as a frequency discriminator, i.e., the power spectral density of the transmission signal at resonance after the reference cell, divided by the slope of error signal at $\Delta_L = 0$. The measured laser frequency noise is presented in Fig. 5 with and w/o frequency locking. In the locking case, the servo bandwidth is about 3 kHz and the noise is found to be reduced by about 25 dB at $f = 125$ Hz (local oscillator modulation frequency in clock operation).

E. Polarization modulation

We studied the response time of the LCPR (FPR-100-895, Meadowlark Optics). As illustrated in Fig. 6, the measured rise (fall) time is about 100 µs and the polarization extinction ratio is about 50. In comparison, the electro-optic amplitude modulator (EOAM) used as polarization modulator in our previous investigations [28] showed a response time of 2.5 µs (limited by our high voltage amplifier) and a polarization extinction ratio of 63. Here, we replace it by a liquid crystal device because its low voltage and small size would be an ideal choice for a compact CPT clock, and we will show in the following that the longer switching time does not limit the contrast of the CPT signal.

F. Microwave source and clock servo-loop

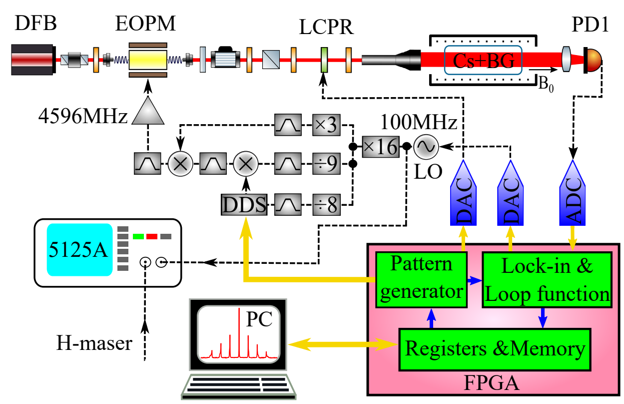

FIG. 7. Electronic architecture of the DM CPT clock: DDS direct digital synthesizer, DAC digital-to-analog converter, ADC analog-to-digital converter, FPGA field programmable gate array, LO local oscillator.

The electronic system (local oscillator and digital electronics for clock operation) used in our experiment is depicted in Fig. 7. The 4.596 GHz microwave source is based on the design described in [37]. The local oscillator (LO) is a module (XM16 Pascall) integrating an ultra-low phase noise 100 MHz quartz oscillator frequency-multiplied without excess noise to 1.6 GHz. The 4.596 GHz signal is synthesized by a few frequency multiplication, division and mixing stages. The frequency modulation and tuning is yielded by a direct digital synthesizer (DDS) referenced to the LO. The clock operation [2, 38] is performed by a single field programmable gate array (FPGA) which coordinates the operation of the DDS, analog-to-digital converters (ADC) and digital-to-analog converter (DACs):

(1) the DDS generates a signal with phase modulation (modulation rate f_m, depth $\pi/2$) and frequency modulation (F_M, depth Δ_{F_M}).

(2) the DAC generates a square-wave signal to drive the LCPR with the same rate f_m, synchronous to the phase modulation.

(3) the ADC is the front-end of the lock-in amplifier. Another DAC, used to provide the feedback to the local oscillator frequency, is also implemented in the FPGA.

The clock frequency is measured by comparing the LO signal with a 100 MHz signal delivered by a H maser of the laboratory in a Symmetricom 5125A Allan deviation test set. The frequency stability of the maser is 1×10^{-13} at 1 s integration time.

III. CLOCK SIGNAL OPTIMIZATION

A. Time sequence and figure of merit

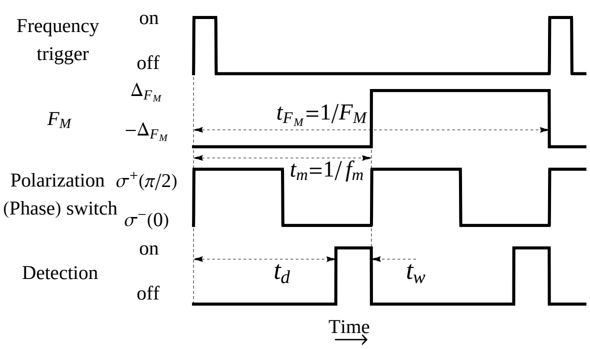

FIG. 8. Time sequence. F_M modulation frequency of the 4.596 GHz signal, f_m polarization and phase modulation frequency, t_d pumping time, t_w detection window.

As illustrated in Fig. 8, the polarization and phase modulation share the same modulation function. After a pumping time t_d to prepare the atoms into the CPT state, we detect the CPT signal with a window of length t_w. Although the detection is sampled, the interrogation is CW, it is why we call our scheme a CW interrogation scheme. In order to get an error signal to close the clock frequency loop, the microwave frequency is square-wave modulated with a frequency F_M, and a depth Δ_{F_M}. In our case, we choose $F_M = 125$ Hz, as a trade-off between a low frequency to have time to accumulate the atomic population into the clock states by the DM scheme and a high operating frequency to avoid low frequency noise in the lock-in amplification process and diminish the intermodulation effects.

A typical experimental CPT signal, recorded with this time sequence, showing all the CPT transitions allowed between Zeeman sub-levels of the Cs ground state is reported in Fig. 9. The Raman detuning Δ is the difference between the two first sideband spacing and the Cs clock resonance. The spectrum shows that the clock levels ($0-0$ transition) are the most populated and that the atomic population is symmetrically distributed around

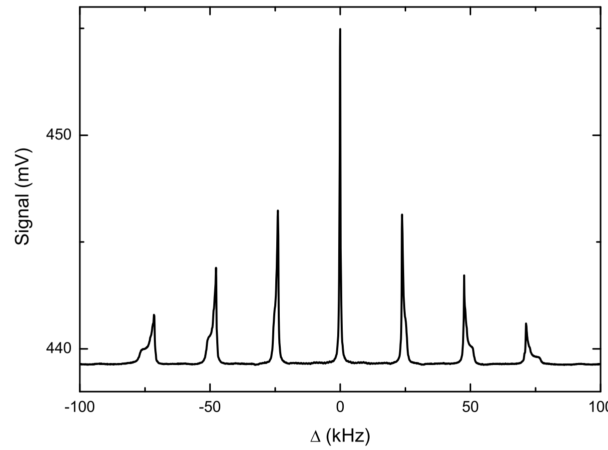

FIG. 9. Zeeman spectrum. The center peak is the $0-0$ clock transition. Working parameters: $t_d = 2\,\mathrm{ms}$, $t_w = 2\,\mathrm{ms}$, $f_m = 500\,\mathrm{Hz}$, $P_L = 163\,\mu\mathrm{W}$, $P_{\mu w} = 26.12\,\mathrm{dBm}$, $T_{cell} = 35.1\,°\mathrm{C}$.

the ($m_F = 0$) sub-levels. The distortion of neighbouring lines is explained by magnetic field inhomogeneities.

It can be shown that the clock short-term frequency stability limited by an amplitude noise scales as W_h/C [10], with W_h the full width at half maximum (FWHM) of the clock resonance, and C the contrast of the resonance. Usually, the ratio of contrast C to W_h is adopted as a figure of merit, *i.e.* $F_C = C/W_h$. The best stability should be obtained by maximizing F_C.

The stability of the clock is measured by the Allan standard deviation $\sigma_y(\tau)$, with τ the averaging time. When the signal noise is white, of variance σ_N^2 in 1 Hz bandwidth, and for a square-wave frequency modulation, the stability limited by the signal-to-noise ratio is equal to [39]

$$\sigma_y(\tau) = \frac{1}{f_c} \frac{\sigma_N}{S_\ell} \sqrt{\frac{1}{\tau}}, \tag{1}$$

with f_c the clock frequency, and S_ℓ the slope of the frequency discriminator. In CPT clocks, one of the main sources of noise is the laser intensity noise, which leads to a signal noise proportional to the signal. Therefore it is more convenient to characterize the quality of the signal of a CPT atomic clock by a new figure of merit, $F_S = S_\ell/V_{wp}$, where S_ℓ is the slope of the error signal (in V/Hz) at Raman resonance ($\Delta = 0$), and V_{wp} is the detected signal value (in V) at the interrogating frequency (the clock resonance frequency plus the modulation depth Δ_{F_M}), see Fig. 10. Note that an estimation of the discriminator slope is also included in F_C, since the contrast is the signal amplitude A divided by the background B. F_C then equals $(A/W_h)/B$, (A/W_h) is a rough approximation of the slope S_ℓ, and B an approximation of the working signal V_{wp}. In our experimental conditions $A/W_h \sim S_\ell/3$.

We investigated the effect of relevant parameters on both figures of merit to optimize the clock performances.

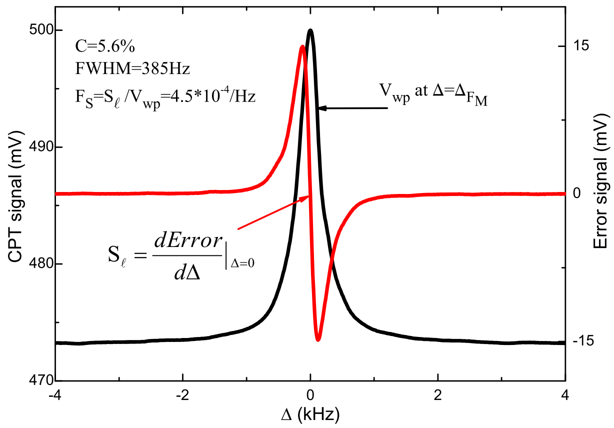

FIG. 10. Signal of the clock transition and error signal. Working parameters: $t_d = 3\,\text{ms}$, $t_w = 1\,\text{ms}$, $f_m = 250\,\text{Hz}$, $P_L = 163\,\mu\text{W}$, $P_{\mu w} = 26.12\,\text{dBm}$, $T_{cell} = 35.1\,°\text{C}$.

In order to allow a comparison despite different conditions, the error signals are generated with the same unit gain. Since the resonance linewidth is also subject to change, it is necessary to optimize the 4.6 GHz modulation depth Δ_{F_M} to maximize F_S. Here for simplicity, we first recorded the CPT signal, then we can numerically compute optimized values of Δ_{F_M} and F_S.

In the following, we investigate the dependence of F_C and F_S on several parameters including the cell temperature (T_{cell}), the laser power (P_L), the microwave power ($P_{\mu w}$), and the polarization (phase) modulation frequency (f_m). The effect of the detection window duration (t_w) and the detection start time (t_d) are presented in Fig. 1 and Fig. 2 respectively of the Supplemental Material [34].

B. Cell temperature and laser power

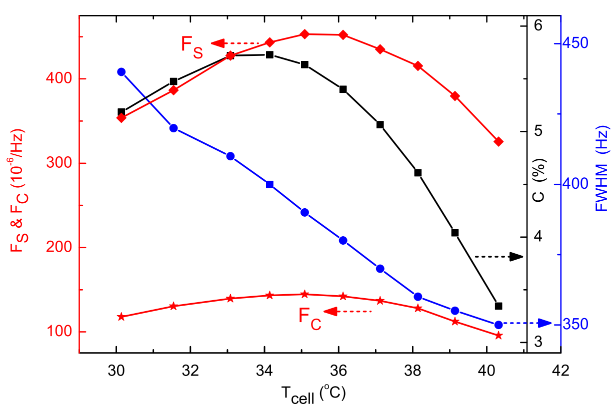

FIG. 11. Figures of merit F_S, F_C, contrast C and width of the clock transition as function of cell temperature T_{cell}. All other working parameters are the same as Fig. 10.

From the figures of merit shown in Fig. 11, the optimized cell temperature is around $T_{cell} = 35.1\,°\text{C}$ for $P_L = 163\,\mu\text{W}$. The narrower linewidth observed at higher T_{cell}, already observed by Godone *et al.* [40], can be explained by the propagation effect: the higher is the cell temperature, the stronger is the light absorption by more atoms, and less light intensity is seen by the atoms at the end side of the vapour cell. This leads to a reduction of the power broadening and a narrower signal measured by the transmitted light amplitude. The optimum temperature depends on the laser power as depicted in Fig. 12. Nevertheless, the overall maximum of F_S is reached with $P_L = 163\,\mu\text{W}$ at $T_{cell} = 35.1\,°\text{C}$.

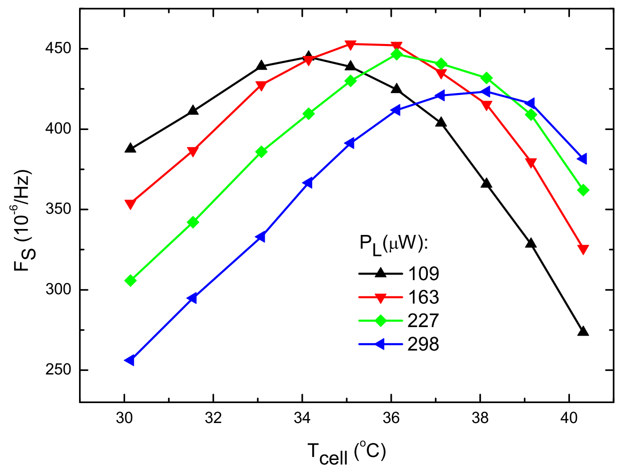

FIG. 12. F_S as a function of cell temperature T_{cell} for various laser powers. All other working parameters are the same as Fig. 10.

The figures of merit F_S, F_C, the contrast C and the width are plotted as a function of the laser power in Fig. 13 for $T_{cell} = 35.1\,°\text{C}$. The laser powers maximizing F_S and F_C are $P_L = 163\,\mu\text{W}$ and $P_L = 227\,\mu\text{W}$, respectively. The Allan deviation reaches a better value at $P_L = 163\,\mu\text{W}$, which justifies our choice of F_S as figure of merit. And in the following parameters investigation, we only show the F_S as figure of merit for clarity.

C. Microwave power

F_S, C and width versus the microwave power are shown in Fig. 14. The behaviour of F_S is basically in agreement with the fractional power of first (±1) sidebands of Fig. 2. The optimized microwave power is around 26.12 dBm.

D. Polarization (phase) modulation frequency f_m

Figure 15 shows F_S, C, and width versus the polarization (phase) modulation frequency f_m The maxima of F_S is reached at low frequency f_m. On one hand, this is an encouraging result to demonstrate the suitability of the LCPR polarization modulator in this experiment. On the other hand, the higher F_M rate would be better for a clock operation with lock-in method to modulate and demodulate the error signal, to avoid the low frequency noises such as $1/f$ noise. Therefore, we chose $F_M = 125\,\mathrm{Hz}$ and $f_m = 250\,\mathrm{Hz}$. We have noticed that the behavior of C is not exactly the same than the one observed in our previous work [41, 42] with a fast EOAM, where the signal amplitude was maximized at higher frequencies. This can be explained by the slower response time of the polarization modulator and the lower laser intensity used. The linewidth reaches a minimum around 1.5 kHz. This behaviour will be investigated in the future.

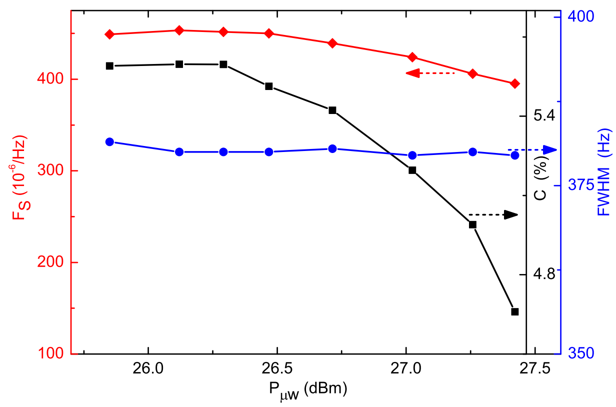

FIG. 14. F_S, C and width of the clock transition as function of microwave power $P_{\mu w}$ with $T_{cell} = 35.1\,°\mathrm{C}$. All other working parameters are the same as Fig. 10.

IV. FREQUENCY STABILITY

A. Measured stability

The high contrast and narrow line-width CPT signal obtained with the optimized values of the parameters is presented in Fig. 10, with the related error signal. The Allan standard deviation of the free-running LO and of the clock frequency, measured against the H maser, are shown in Fig. 16. The former is in agreement with its measured phase noise. In the 1 Hz to 100 Hz offset frequency region, the phase noise spectrum of the free-running 4.596 GHz LO signal is given in dBrad^2/Hz by $S_\varphi(f) = b_{-3}f^{-3}$ with $b_{-3} = -47$, signature of a flicker frequency noise [37]. This phase noise yields an expected Allan deviation given by $\sigma_y(1\,\mathrm{s}) \approx \sqrt{2\ln 2 \times \frac{4b_{-3}}{f_c^2}} \approx 1.2\times10^{-12}$ [43], close to the measured value of 2×10^{-12} at 1 s. The measured stability of the CPT clock is $3.2\times10^{-13}\tau^{-1/2}$ up to 100 s averaging time for our best record. This value is close to the best CPT clocks [31, 33], demonstrating that a high-performance CPT clock can be built with the DM-CPT scheme. A typical record for longer averaging times is also shown in Fig. 16. For averaging times τ longer than 20 s, the Allan deviation increases like $\sqrt{\tau}$, signature of a random walk frequency noise.

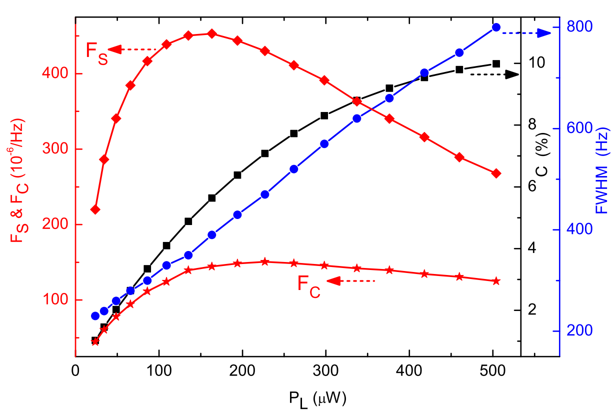

FIG. 13. F_S, F_C, C and width of the clock transition as a function of laser power P_L with $T_{cell} = 35.1\,°\mathrm{C}$. All other working parameters are the same as Fig. 10.

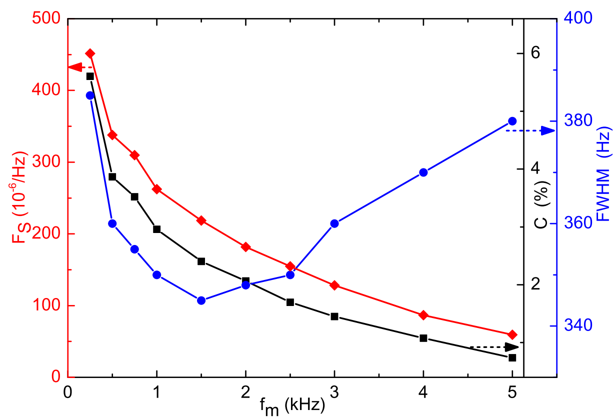

FIG. 15. F_S, C and width of the clock transition as function of f_m. All other working parameters are the same as Fig. 10.

B. Short-term stability limitations

We have investigated the main noise sources that limit the short-term stability. For a first estimation, we consider only white noise sources, and for the sake of simplicity we assume that the different contributions can independently add, so that the total Allan variance can be computed as

$$\sigma_y^2(\tau) = \Sigma_i \sigma_{y,p_i}^2(\tau) + \sigma_{y,LO}^2(\tau), \tag{2}$$

with $\sigma_{y,LO}^2(\tau)$ the contribution due to the phase noise of the local oscillator, and $\sigma_{y,p_i}^2(\tau)$ the Allan variance of the clock frequency induced by the fluctuations of the parameter p_i. When p_i modifies the clock frequency during the whole interrogation cycle, $\sigma_{y,p_i}^2(\tau)$ can be written as

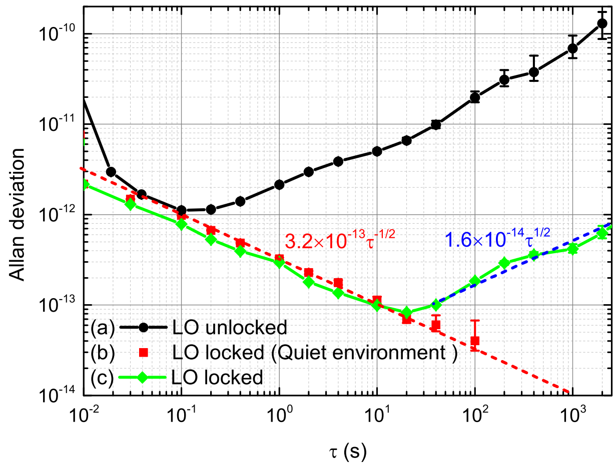

FIG. 16. The LO frequency stability (a) free running, (b) and (c) locked on the atomic resonance. (b) best record in quiet environment, (c) typical record. The slope of the red (blue) dashed fitted line is $3.2\times10^{-13}\tau^{-1/2}$ ($1.6\times10^{-14}\tau^{1/2}$), respectively.

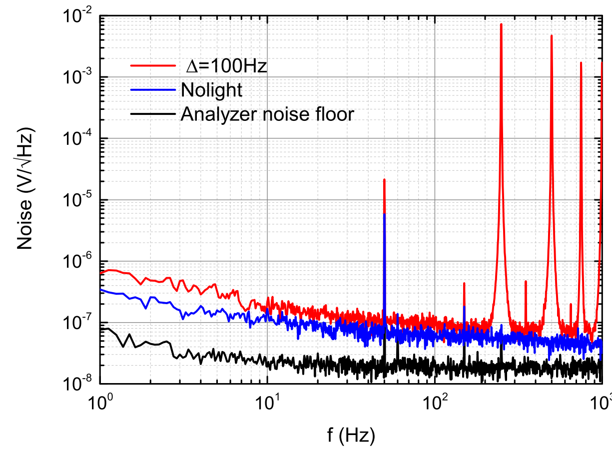

FIG. 17. The RIN after the cell, detector noise and analyser noise floor. Working parameters are the same as Fig. 10.

$$\sigma^2_{y,p_i}(\tau) = \frac{1}{f_c^2}\left(\sigma^2_{p_i}\right)_{1Hz}\left(\delta f_c/\delta p_i\right)^2\frac{1}{\tau}, \quad (3)$$

with $\left(\sigma^2_{p_i}\right)_{1Hz}$ the variance of p_i measured in 1 Hz bandwidth at the modulation frequency F_M, $(\delta f_c/\delta p_i)$ is the clock frequency sensitivity to a fluctuation of p_i. Here, the detection signal is sampled during a time window t_w with a sampling rate $2F_M = 1/T_c$, where T_c is a cycle time. In this case Eq.(3) becomes

$$\sigma^2_{y,p_i}(\tau) = \frac{1}{f_c^2}\left(\sigma^2_{p_i}\right)_{tw}\left(\delta f_c/\delta p_i\right)^2\frac{T_c}{\tau}, \quad (4)$$

with $\left(\sigma^2_{p_i}\right)_{tw}$ the variance of p_i sampled during t_w; $\left(\sigma^2_{p_i}\right)_{tw} \approx S_{p_i}(F_M)/(2t_w)$ with $S_{p_i}(F_M)$ the value of the power spectral density (PSD) of p_i at the Fourier frequency F_M (assuming a white frequency noise around F_M). When p_i induces an amplitude fluctuation with a sensitivity $(\delta V_{wp}/\delta p_i)$, Eq.(4) becomes

$$\sigma^2_{y,p_i}(\tau) = \frac{1}{f_c^2}S_{p_i}(F_M)\frac{\left(\delta V_{wp}/\delta p_i\right)^2}{S_\ell^2}\frac{T_c}{2t_w}\frac{1}{\tau}, \quad (5)$$

with S_ℓ the slope of the frequency discriminator in V/Hz. We review below the contributions of the different sources of noise.

Detector noise: the square root of the power spectral density (PSD) S_d of the signal fluctuations measured in the dark is shown in Fig. 17. It is $N_{detector} = 64.8$ nV/$\sqrt{\text{Hz}}$ in 1 Hz bandwidth at the Fourier frequency 125 Hz. According to Eq.(5) the contribution of the detector noise to the Allan deviation at one second is 0.45×10^{-13}.

Shot-noise: with the transimpedance gain $G_R = 1.5\times10^4\,\text{V A}^{-1}$ and the detector current $I = V_{wp}/G_R = 32.7\,\mu\text{A}$, Eq.(5) becomes

$$\sigma^2_{y,sh}(\tau) = \frac{1}{f_c^2}\frac{\left(2eIG_R\right)^2}{S_\ell^2}\frac{T_c}{2t_w}\frac{1}{\tau}, \quad (6)$$

with e the electron charge. The contribution to the Allan deviation at one second is 0.34×10^{-13}.

Laser FM-AM noise: it is the amplitude noise induced by the laser carrier frequency noise. The slope of the signal V_{wp} with respect to the laser frequency f_L is $S_{FM-AM} = 0.16\,\text{mV MHz}^{-1}$ at optical resonance. According to Eq.(5) with data of laser-frequency-noise PSD of Fig. 5 at 125 Hz, we get a Allan deviation of 0.33×10^{-13} at one second.

Laser AM-AM noise: it is the amplitude noise induced by the laser intensity noise. The measured signal sensitivity to the laser power is $S_{AM} = 3.31\,\text{mV}\,\mu\text{W}^{-1}$ at $f_L = 163\,\mu\text{W}$, combined with the laser intensity PSD of Fig. 3 it leads to the amplitude noise $S_{AM}\times P_L\times RIN(125\,\text{Hz}) = 30.3\text{ nV}/\sqrt{\text{Hz}}$, and an Allan deviation of 0.21×10^{-13} at one second.

LO phase noise: the phase noise of the local oscillator degrades the short-term frequency stability via the intermodulation effect [44]. It can be estimated by:

$$\sigma_{y_{LO}}(1s) \sim \frac{F_M}{f_c}\sqrt{S_\varphi(2F_M)}. \quad (7)$$

Our 4.596 GHz microwave source is based on [37] which shows an ultra-low phase noise $S_\varphi(2F_M) = -116\,\text{dB rad}^2\,\text{Hz}^{-1}$ at $2F_M = 250$ Hz Fourier frequency. This yields a contribution to the Allan deviation of 0.43×10^{-13} at one second.

Microwave power noise: fluctuations of microwave power lead to a laser intensity noise, which is already taken into account in the RIN measurement. We show in the next section that they also lead to a frequency shift (see Fig. 20). The Allan deviation of the microwave power at 1 s is 2.7×10^{-4} dBm, see inset of Fig. 20. With a measured slope of 7.7 Hz/dBm, we get a fractional-frequency Allan deviation of 2.26×10^{-13}, which is the largest contribution to the stability at 1 s. Note that in our set-up the microwave power is not stabilized.

The other noise sources considered have much lower contributions, they are the laser frequency-shift effect, *i.e.* AM-FM and FM-FM contributions, the cell temperature and the magnetic field. Table I resumes the short-term stability noise budget.

TABLE I. Noise contributions to the stability at 1 s.

Noise source	noise level	$\sigma_y(1s) \times 10^{13}$
Detector noise	$64.8\,\mathrm{nV}/\sqrt{\mathrm{Hz}}$	0.45
Shot noise	$48.8\,\mathrm{nV}/\sqrt{\mathrm{Hz}}$	0.34
Laser FM-AM	$48.0\,\mathrm{nV}/\sqrt{\mathrm{Hz}}$	0.33
Laser AM-AM	$30.3\,\mathrm{nV}/\sqrt{\mathrm{Hz}}$	0.21
LO phase noise	$-116\,\mathrm{dBrad}^2/\mathrm{Hz}$	0.43
$P_{\mu w}$	2.7×10^{-4} dBm@1 s	2.26
Laser AM-FM	0.6 nW@1 s	9.7×10^{-3}
Laser FM-FM	~ 100 Hz@1 s	2.9×10^{-3}
T_{cell}	6.3×10^{-5} K@1 s	3.2×10^{-2}
B_0	4.3 pT@1 s	1.4×10^{-3}
Total		2.4

The laser intensity noise after interacting with the atomic vapor is depicted in Fig. 17. It encloses the different contributions to the amplitude noise, *i.e.* detector noise, shot-noise, FM-AM and AM-AM noises. The noise spectral density is $100\,\mathrm{nV}/\sqrt{\mathrm{Hz}}$ at the Fourier frequency 125 Hz, which leads to an Allan deviation of 0.7×10^{-13} at 1 s. This value is equal to the quadratic sum of the individual contributions. The quadratic sum of all noise contribution leads to an Allan deviation at one second of 2.4×10^{-13}, while the measured stability is $3.2 \times 10^{-13}\tau^{-1/2}$ (Fig. 16). The discrepancy could be explained by correlations between different noises, which are not all independent. The dominant contribution is the clock frequency shift induced by the microwave power fluctuations. This term could be reduced by microwave power stabilization or a well chosen laser power (see Fig. 14), but to the detriment of the signal amplitude.

V. FREQUENCY SHIFTS AND MID-TERM STABILITY

We have investigated the clock-frequency shift f_0 with respect to the variation of various parameters, with the definition $f_0 = f_c - f_{Cs}$, f_{Cs} is the unperturbed Cs atom clock frequency 9.192 631 770 GHz. Here we address the polarization (phase) modulation frequency f_m, the laser power P_L and the microwave power $P_{\mu w}$ induced clock-frequency shift. The other parameters measurements can be found from Fig. 3 to Fig. 5 in the Supplemental Material [34]. For each frequency measurement, the LO frequency is locked on the CPT resonance. With a 100 s averaging time, the mean frequency is measured with typical error bar less than 10^{-12}, *i.e.*, 0.01 Hz relative to the Cs frequency f_{Cs}.

A. f_0 vs f_m

In order to get more insight into the physics involved in our experiment, we have measured the clock shift versus polarization (phase) modulation frequency f_m. Results are reported in Fig. 18. The oscillatory behaviour is not fully understood yet, we are going to investigate it theoretically by taking into consideration the slow response time [41] of our LCPR in the future. When other parameters are fixed, the shift coefficient is $3.17\,\mathrm{mHz\,Hz^{-1}}$ at $f_m = 250$ Hz. As f_m is synchronized to the LO, which exhibits in the worst case (unlocked) a frequency stability at the level of 7×10^{-11} at 1000 s (see Fig. 16), the effect of the polarization and phase modulation frequency on the clock shift is negligible, *i.e.* 6.0×10^{-21} at 1000 s second.

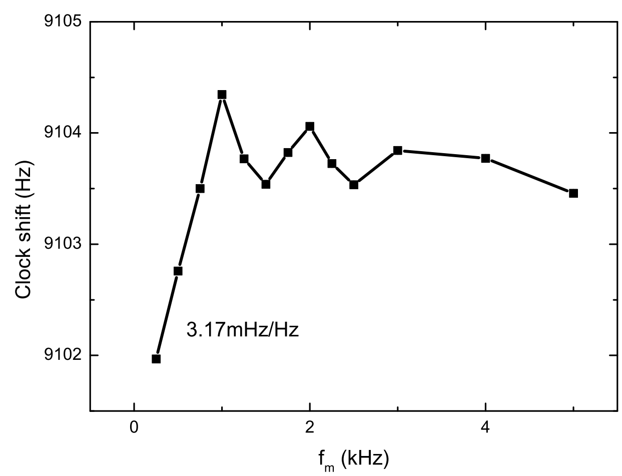

FIG. 18. Clock frequency as function of polarization(phase) modulation frequency f_m. All other working parameters are the same as Fig. 10.

B. f_0 vs P_L

The clock frequency shift versus P_L is presented in Fig. 19. The coefficient of the light power shift is $14.9\,\mathrm{Hz\,mW^{-1}}$ at $P_L = 163\,\mu\mathrm{W}$ and $P_{\mu w} = 26.12$ dBm. This shift is difficult to foresee theoretically because it results not only from the combination of light shifts (AC Stark shift) induced by all sidebands of the optical spectrum, but also from the overlapping and broadening of neighboring lines. The inset of Fig. 19 shows the typical fractional fluctuations the laser power versus the integration time. They are measured to be 1×10^{-4} at 1000 s, impacting on the clock fractional frequency stability at the level of 2.6×10^{-14} at 1000 s. Since the power distribution in the sidebands vary with the microwave power, the laser power shift is also sensitive to the microwave power feeding the EOPM. This is clearly shown in Fig. 19. As previously observed in CPT-based clocks [45, 46] and double-resonance Rb clocks [47], it is important to note that the light-power shift coefficient can be decreased and even cancelled at specific values of $P_{\mu w}$. Consequently, it should be possible to improve the long-term frequency stability by tuning finely the microwave power value [48, 49], at the expense of a slight degradation of the short-term frequency stability.

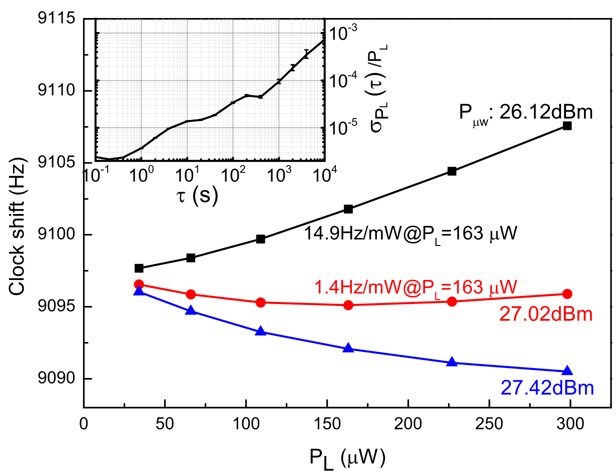

FIG. 19. Clock frequency as a function of laser power P_L for different values of $P_{\mu w}$. Inset: fractional Allan deviation of the laser power. All other working parameters are the same as Fig. 10.

C. f_0 vs $P_{\mu w}$

The frequency shift versus the microwave power at various laser power is shown on Fig. 20. At constant optical power, only the power distribution among the different sidebands changes. The shift scales as the microwave power in the investigated range, with a sensitivity of $7.7\,\mathrm{Hz\,dBm^{-1}}$ at $P_L = 163\,\mu\mathrm{W}$. In this range, the power ratio of both first (±1) sidebands changes by about 10%. The inset of Fig. 20 shows the Allan deviation of the microwave power in dBm. The typical microwave power standard deviation of 5×10^{-4} dBm at 1000 s yields a fractional frequency stability of about 4.2×10^{-13} at 1000 s.

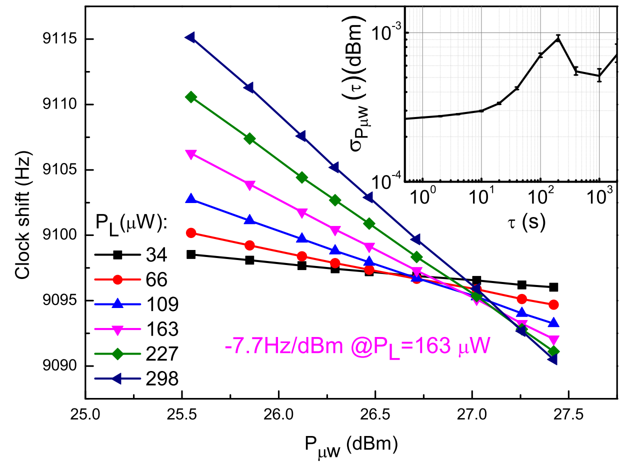

FIG. 20. Clock frequency as a function of the microwave power $P_{\mu w}$ at various laser power. Inset: Allan deviation of the microwave power in dBm, log scale. All other working parameters are the same as Fig. 10.

D. Mid-term stability

With the shift coefficients and the Allan standard deviation of the involved parameters, we can estimate the various contributions to the mid-term clock frequency stability. They are listed in Table II for a 1000 s averaging time. Their quadratic sum leads to a frequency stability of 4.2×10^{-13} at $\tau = 1000$ s, in very good agreement with the measured stability 4.21×10^{-13} (see Fig. 16). Again, the main contribution to the instability comes from the microwave power fluctuations, before the laser power and frequency fluctuations. Thus in the future, it is necessary to stabilize the microwave power to improve both the short-and-mid-term frequency stability.

TABLE II. Noise contributions to the stability at 1000 s.

Parameter	coefficient	$\sigma_y(1000s) \times 10^{13}$
T_{cell}	$0.47\,\mathrm{Hz\,K^{-1}}$	2.7×10^{-2}
P_L	$14.9\,\mathrm{Hz\,mW^{-1}}$	0.26
$P_{\mu w}$	$-7.7\,\mathrm{Hz\,dBm^{-1}}$	4.2
Δ_L	$-26.6\,\mathrm{mHz\,MHz^{-1}}$	0.14
B_0	$0.29\,\mathrm{Hz\,\mu T^{-1}}$	0.4×10^{-2}
Total		4.2

VI. CONCLUSIONS

We have implemented a compact vapor cell atomic clock based on the DM CPT technique. A detailed characterization of the CPT resonance versus several experimental parameters was performed. A clock frequency stability of $3.2 \times 10^{-13}\tau^{-1/2}$ up to 100 s averaging time was demonstrated. For longer averaging times, the Allan deviation scales as $\sqrt{\tau}$, signature of a random walk frequency noise. It has been highlighted that the main limitation to the clock short and mid-term frequency stability is the fluctuations of the microwave power feeding the EOPM. Improvements could be achieved by implementing a microwave power stabilization. Another or complementary solution could be to choose a finely tuned laser power value minimizing the microwave power sensitivity. This adjustment could be at the expense of the signal reduction and a trade-off has to be found. Nevertheless, the recorded short-term stability is already at the level of best CPT clocks [31, 33] and close to state-of-the art Rb vapor cell frequency standards. These preliminary results show the possibility to a high-performance and compact CPT clock based on the DM-CPT technique.

ACKNOWLEDGEMENTS

We thank Moustafa Abdel Hafiz (FEMTO-ST), David Holleville and Luca Lorini (LNE-SYRTE) for helpful discussions. We are also pleased to acknowledge Charles Philippe and Ouali Acef for supplying the thermal insulation material, Michel Abgrall for instrument Symmetricom 5125A lending, David Horville for laboratory arrangement, José Pinto Fernandes, Michel Lours for electronic assistance, Pierre Bonnay and Annie Gérard for manufacturing Cs cells.

P. Y. is supported by the Facilities for Innovation, Research, Services, Training in Time & Frequency (LabeX FIRST-TF). This work is supported in part by ANR and DGA(ISIMAC project ANR-11-ASTR-0004). This work has been funded by the EMRP program (IND55 Mclocks). The EMRP is jointly funded by the EMRP participating countries within EURAMET and the European Union.

[1] J. Camparo, The rubidium atomic clock and basic research, Physics Today, pp 33–39 (November 2007).

[2] S. Micalizio, C. E. Calosso, A. Godone and F. Levi, Metrological characterization of the pulsed Rb clock with optical detection, Metrologia **49**, 425-436 (2012).

[3] T. Bandi, C. Affolderbach, C. Stefanucci, F. Merli, A. K. Skrivervik and G. Mileti, Compact high-performance continuous-wave double-resonance rubidium standard with $1.4 \times 10^{-13}\tau^{-1/2}$ stability, IEEE Ultrason. Ferroelec. Freq. Contr. **61**, 11, 1769–1778 (2014).

[4] S. Kang, M. Gharavipour, C. Affolderbach, F. Gruet, and G. Mileti, Demonstration of a high-performance pulsed optically pumped Rb clock based on a compact magnetron-type microwave cavity, J. Appl. Phys. **117**, 104510 (2015).

[5] A. Godone, F. Levi, C. E. Calosso and S. Micalizio, High-performing vapor cell frequency standards, Rivista di Nuovo Cimento **38**, 133-171 (2015).

[6] G. Alzetta, A. Gozzini, L. Moi, and G. Orriols, An experimental method for the observation of R. F. transitions and laser beat resonances in oriented Na vapour, Il Nuovo Cimento **36 B**, 5 (1976).

[7] E. Arimondo, Coherent population trapping in laser spectroscopy, Progress in Optics **35**, 257-354 (1996).

[8] K. Bergmann, H. Theuer, and B. W. Shore, Coherent population transfer among quantum states of atoms and molecules. Rev. Mod. Phys., **70**, 1003-1025 (1998).

[9] R. Wynands and A. Nagel, Precision spectroscopy with coherent dark states, Appl. Phys. **B 68**, 1 (1999).

[10] J. Vanier, Atomic clocks based on coherent population trapping: A review, Appl. Phys. B **81**, 421-442 (2005).

[11] M. Bajcsy, A. S. Zibrov and M. D. Lukin, Stationary pulses of light in an atomic medium, Nature **426,** 638-641 (2003).

[12] P. D. D. Schwindt, S. Knappe, V. Shah, L. Hollberg, J. Kitching, L. A. Liew and J. Moreland, Chip-scale atomic magnetometer, Appl. Phys. Lett. **85,** 26, 6409-6411 (2004).

[13] E. Breschi, Z. D. Gruji, P. Knowles and A. Weis, A high-sensitivity push-pull magnetometer, Appl. Phys. Lett. **104,** 023501 (2014).

[14] A. Aspect, E. Arimondo, R. Kaizer, N. Vansteenkiste and C. Cohen-Tannoudji, Transient velocity-selective coherent population trapping in one dimension, J. Opt. Soc. Am. B **6**, 2112-2124 (1989).

[15] J. Vanier and C. Mandache, The passive optically pumped Rb frequency standard: The laser approach, Appl. Phys. B Lasers Opt. **87**, 565-593 (2007).

[16] J. E. Thomas, S. Ezekiel, C. C. Leiby, R. H. Picard, and C. R. Willis, Ultrahigh-resolution spectroscopy and frequency standards in the microwave and far-infrared regions using optical lasers, Opt. Lett. **6**, 298-300 (1981).

[17] J. E. Thomas, P. R.Hemmer, S. Ezekiel, C. C. Leiby,, R. H. Picard, and C. R. Willis, Observation of Ramsey fringes using a stimulated, resonance Raman transition in a sodium atomic beam, Phys. Rev. Lett. **48**, 867-870 (1982).

[18] N. Cyr, M. Tetu, and M. Breton, All-optical microwave frequency standard - a proposal, IEEE Trans. Instrum. Measur. **42**, 640-649 (1993).

[19] J. Kitching, N. Vukicevic, L. Hollberg, S. Knappe, R.Wynands, and W. Weidemann, A microwave frequency reference based on VCSEL-driven dark line resonances in Cs vapor, IEEE Trans. Instrum. Measur. **49**, 1313-1317 (2000).

[20] J. Kitching, L. Hollberg, S. Knappe, and R. Wynands, Compact atomic clock based on coherent population trapping, Electron. Lett. **37**, 1449 (2001).

[21] J. Kitching, S. Knappe, and L. Hollberg, Miniature vapor-cell atomic-frequency references, Appl. Phys. Lett. **81**, 553 (2002).

[22] L. Liew, S. Knappe, J. Moreland, H. Robinson, L. Hollberg, and J. Kitching, Microfabricated alkali atom vapor cells, Appl. Phys. Lett. **84**, 2694 (2004).

[23] S. Knappe, V. Shah, P. D. D. Schwindt, L. Hollberg, J. Kitching, L.-A.Liew, and J. Moreland, A microfabricated

atomic clock, Appl. Phys. Lett. **85**, 1460 (2004).
[24] http://www.microsemi.com/products/timing-synchronizationsystems/embedded-timing-solutions/components/sa-45s-chip-scale-atomic-clock#resources
[25] http://www.inrim.it/Mclocks
[26] V. Shah and J. Kitching, Advances in coherent population trapping for atomic clocks, in Advances in Atomic, Molecular,and Optical Physics, edited by E. Arimondo, P. R. Berman, and C. C. Lin, Vol. 59 (Elsevier, Amsterdam, 2010).
[27] Peter Yun, Doctor thesis, Exploring New Approaches to Coherent Population Trapping Atomic Frequency Standards, Wuhan Institute of Physics and Mathematics Chinese Academy of Sciences, Wuhan, China, 2012.
[28] P. Yun, J.-M. Danet, D. Holleville, E. de Clercq, and S. Guérandel, Constructive polarization modulation for coherent population trapping clock, Appl. Phys. Lett. **105**, 231106 (2014).
[29] Y.-Y. Jau, E. Miron, A. B. Post, N. N. Kuzma, and W. Happer, Push-Pull Optical Pumping of Pure Superposition States, Phys. Rev. Lett. **93**, 160802-1-4 (2004).
[30] X. Liu, J.-M. Mérolla, S. Guérandel, C. Gorecki, E. de Clercq, and R. Boudot, Coherent population trapping resonances in buffer-gas-filled Cs-vapor cells with push-pull optical pumping, Phys. Rev. A **87**, 013416 (2013).
[31] M. Abdel Hafiz and R. Boudot, A coherent population trapping Cs vapor cell atomic clock based on push-pull optical pumping, J. Appl. Phys. **118**, 124903 (2015).
[32] T. Zanon, S. Guérandel, E. de Clercq, D. Holleville, N. Dimarcq and A. Clairon, High Contrast Ramsey Fringes with Coherent-Population-Trapping Pulses in a Double Lambda Atomic System, Phys. Rev. Lett. **94,** 193002 (2005).
[33] J.-M. Danet, O. Kozlova, P. Yun, S. Guérandel and E. de Clercq, Compact atomic clock prototype based on coherent population trapping, EPJ Web of Conferences **77**, 00017 (2014).
[34] See Supplemental Material at http://link.aps.org/supplemental for additional parameters measurement results.
[35] R.Schmeissner, N. von Bande , A.Douahi, O.Parillaud, M.Garcia, M.Krakowski, M.Baldy, The optical feedback spatial phase driving perturbations of DFB laser diodes in an optical clock, Proceedings of the 2016 European Frequency and Time Forum, York (2016), available at http://www.eftf.org/previousmeetings.php.
[36] M. Abdel Hafiz, G. Coget, E. De Clercq, R. Boudot, Doppler-free spectroscopy on the Cs D_1 line with a dual-frequency laser, Opt. Lett. **41**, 2982-2985 (2016).
[37] B. François, C. E. Calosso, M. Abdel Hafiz, S. Micalizio, and R. Boudot, Simple-design ultra-low phase noise microwave frequency synthesizers for high-performing Cs and Rb vapor-cell atomic clocks, Rev. Sci. Instrum. **86**, 094707 (2015).
[38] C. E. Calosso, S. Micalizio, A. Godone, E. K. Bertacco, F. Levi. Electronics for the pulsed rubidium clock: Design and characterization. IEEE Trans. Ultrason. Ferroelectr. Freq. Control **54**, 1731-1740 (2007).
[39] J. Vanier and C. Audoin, *The quantum physics of atomic frequency standards* (Adam Hilger, Bristol, 1989).
[40] A. Godone, F. Levi, S. Micalizio, and J. Vanier, Dark-line in opticall-thic vapors: inversion phenomena and line width narrowing, Eur. Phys. J. D **18**, 5-13 (2002).
[41] P. Yun, S. Guérandel, and E. de Clercq , Coherent population trapping with polarization modulation, J. Appl. Phys. 119, 244502 (2016).
[42] P. Yun, S. Mejri, F. Tricot, M. Abdel Hafiz, R. Boudot, E. de Clercq, S. Guérandel, Double-modulation CPT cesium compact clock, 8th Symposium on Frequency Standards and Metrology 2015, J. of Physics: Conference Series **723**, 012012 (2016).
[43] Enrico Rubiola, Phase noise and frequency stability in oscillators, Cambridge University Press, 2009.
[44] C. Audoin, V. Candelier, and N. Dimarcq, A limit to the frequency stability of passive frequency standards due to an intermodulation effect, IEEE Trans. Instrum. Meas. **40**, 121 (1991).
[45] F. Levi, A. Godone, J. Vanier, The light-shift effect in the coherent population trapping cesium maser, IEEE Trans. Ultrason. Ferroelectr. Freq. Control **47**, 466 (2000).
[46] M. Zhu and L.S. Cutler, Theoretical and experimental study of light shift in a CPT-based Rb vapor cell frequency standard, in Proceedings of the 32nd Precise Time and Time Interval Systems and Applications Meeting, p. 311, ed. by L.A. Breakiron (US Naval Observatory, Washington, DC, 2000).
[47] C. Affolderbach, C. Andreeva, S. Cartaleva, T. Karaulanov, G. Mileti, and D. Slavov, Light-shift suppression in laser optically pumped vapour-cell atomic frequency standards, Appl. Phys. B **80**, 841-8 (2005).
[48] V. Shah, V. Gerginov, P. D. D. Schwindt, S. Knappe, L. Hollberg and J. Kitching, Continuous light- shift correction in modulated coherent population trapping clocks, Appl. Phys. Lett. **89,** 151124 (2006).
[49] B. H. McGuyer, Y. Y. Jau and W. Happer, Simple method of light-shift suppression in optical pumping systems, Appl. Phys. Lett. **94**, 251110 (2009).
[50] O. Kozlova, S. Guérandel, and E. de Clercq, Temperature and pressure shift of the Cs clock transition in the presence of buffer gases: Ne, N_2, Ar, Phys. Rev. A **83**, 062714 (2011).
[51] O. Kozlova, J-M. Danet, S. Guérandel, and E. de Clercq, Limitations of long-term stability in a coherent population trapping Cs Clock, IEEE Trans. Instrum. Meas. **63**, 1863 (2014).